—Electronic Supporting Information for— Influence of Inversion on Mg Mobility and Electrochemistry in Spinels

Gopalakrishnan Sai Gautam,[*,†,‡,¶] Pieremanuele Canepa,[‡,¶] Alexander Urban,[‡] Shou-Hang Bo,[‡,‖] and Gerbrand Ceder[*,§,‡]

† *Department of Materials Science and Engineering, Massachusetts Institute of Technology, Cambridge, MA 02139, USA*

‡ *Materials Sciences Division, Lawrence Berkeley National Laboratory, Berkeley, CA 94720, USA*

¶ *Equally contributed to the work*

§ *Department of Materials Sciences and Engineering, University of California Berkeley, CA 94720, USA*

‖ *Current affiliation: University of Michigan-Shanghai Jiao Tong University Joint Institute, Shanghai Jiao Tong University, Shanghai, 200240, P. R. China*

E-mail: gautam91@mit.edu; gceder@berkeley.edu,gceder@lbl.gov

1 Synthesis and structure of inverse-$MgIn_2S_4$

Elemental forms of Mg (Sigma Aldrich $\geq$ 99%), In (Sigma Aldrich, 99.999% trace metal basis) and S (Sigma Aldrich 99.99% trace metal basis) are first weighted with the stoichiometric ratio. Approximately 2 g of the powder mixture was placed into a tungsten carbide ball mill jar, and the mixture was ball milled (SpexSamplePrep 8000M) for 30 minutes. The resulting powder was then pressed into pellets of 6.0 mm in diameter under a pressure of 1.4 metric tons for 1–2 minutes. Typically, less than 3 pellets, each weighted at $\sim$ 0.2 g, were wrapped into a platinum foil (Sigma Aldrich, 99.99% trace metal basis) which was subsequently secured into a stainless-steel tube (Swagelok, 3/8-inch diameter). The tube was later closed with stainless steel caps, to avoid air exposure during the transfer of the tube for synthesis. All the aforementioned steps were performed in an Ar glove box.

The reaction to form the spinel was carried out in a Thermo Scientific Minimite furnace under a continuous flow of Ar gas. To further reduce the level of oxygen and moisture in the Ar gas, an oxygen/moisture trap was attached between the Ar gas cylinder and the quartz tube where the stainless-steel tube was placed. After a quick purge of Ar ($\sim$ 20 min), the temperature was quickly ramped to 800 °C in 1 hour. The temperature was held at 800 °C for 12 hours, before the furnace was slowly cooled down to room temperature over 50 hours. The powder was collected in Ar glove box by cutting the stainless-steel tube.

The structure of $MgIn_2S_4$ was refined using the Rietveld method. The diffraction pattern of $MgIn_2S_4$ can be readily indexed with the spinel lattice (*Fd-3m*, a = b = c = 10.72060 Å). When the site occupancies of Mg, In and S were fixed to 1.0 while allowing other structural parameters to vary, substantial deviation between the simulated and observed patterns was observed, suggesting that the as-prepared $MgIn_2S_4$ is not a normal spinel. Mg and In site inversion was then tested by allowing simultaneous presence of Mg and In on the same site and by constraining each cation site to be fully occupied and the composition to be $MgIn_2S_4$. Excellent agreement between the calculated and observed data was achieved. The refinement results show that the 8*a* site is occupied by 15% Mg and 85% In, and the 16*d* site

is occupied by 43% Mg and 57% In, corresponding to a degree of inversion, $i = 0.85$. The fitting is presented in Figure S1. Structural parameters from the refinement are tabulated in Tables S1–S3.

Table S1: Crystallographic data for $MgIn_2S_4$ based on the Rietveld refinement of the synchrotron X-ray data.

Radiation	Synchrotron X-ray (11 BM, APS)
Crystal System	Cubic
Space group	*Fd-3m*:2 (#227)
Lattice parameters	a = b = c = 10.72060(4) Å
Cell volume	1232.13(1) $Å^3$
Density (calculated)	4.12066 g/cm^3
λ	0.414173 Å
R_{wp}	12.955%
R_p	10.286%
χ^2	1.190

Table S2: Atomic site information for $MgIn_2S_4$. The thermal parameters (column B_{iso}) should be associated with large errors due to the large absorption of the sample ($\mu R = 4.38$)

Atom	Wyck.	x/a	y/b	z/c	Occ.	B_{iso} ($Å^2$)
S	32e	0.24259(1)	0.24259(1)	0.24259(1)	1	1.35(2)
$M1$	16d	1/2	1/2	1/2	In = 0.57 Mg = 0.43	6.8(5)
$M2$	8a	1/8	1/8	1/8	In = 0.85 Mg = 0.15	1.41(2)

Table S3: Selected bond distances (Å) for $MgIn_2S_4$.

$M1$–S (×6)	2.601(1)
$M2$–S (×4)	2.462(2)

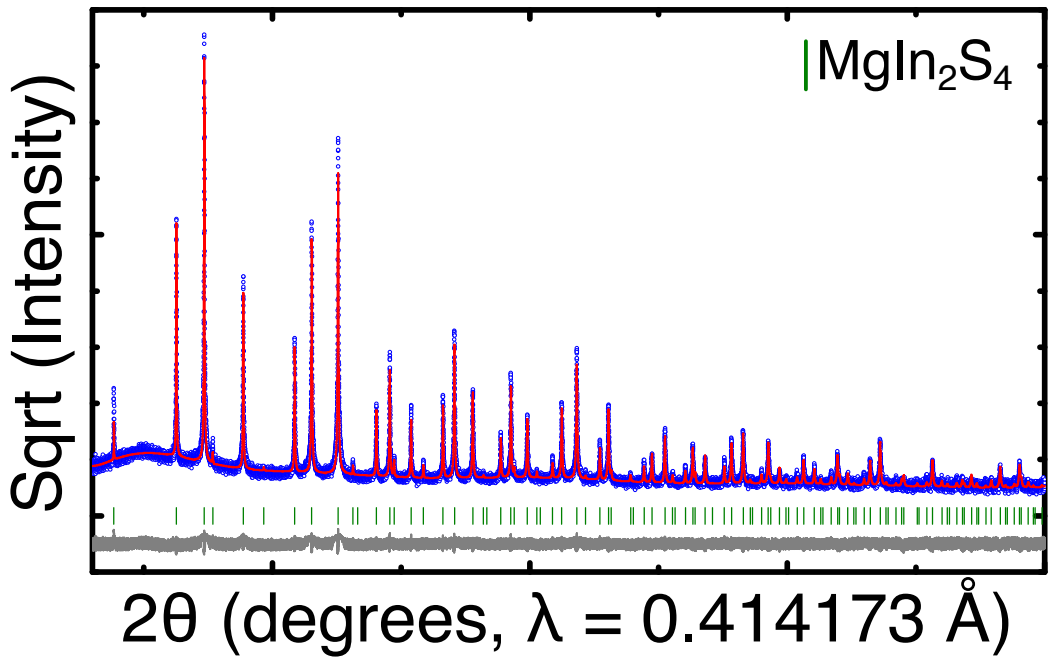

Figure S1: Rietveld refinement of the synchrotron XRD pattern for $MgIn_2S_4$. Data was collected at beamline 11 BM of the Advanced Photon Source, Argonne National Laboratory, with a wavelength of 0.414173 Å. The square root of the intensity is plotted on the y-axis. The observed and calculated curves are shown in blue and red, with the difference curve shown in dark grey. Reflections corresponding to $MgIn_2S_4$ are shown as green tick marks.

2 Convergence of Nudged Elastic Band barriers

Figure S2 plots the change in the activation barriers for Mg diffusion, calculated based on Density Functional Theory (DFT)-based Nudged Elastic Band (NEB) calculations, with the size of the spinel cell used. The parameters used in the calculations are as described in the Methods section of the manuscript. The calculations are performed along the $16d-48f-16d$ ($oct-tet-oct$) trajectory, with the edge-sharing $8a$ site occupied by Mn (Hop 4 in Figure 2 in the main text) in the $Mg_xMn_2O_4$ spinel structure. The corner-sharing $8a$ sites in both calculations are also occupied by cations.

Data from the calculations indicate the Mg^{2+} diffusion barrier, as computed in a 1×1×1 conventional spinel cell ($\sim$ 1418 meV, solid red line in Figure S2) is comparable to a barrier calculated in a larger 2×1×1 cell ($\sim$ 1449 meV, dashed red line, $<$ 3% change), demonstrating that NEB calculations in a conventional spinel cell can provide accurate estimations of

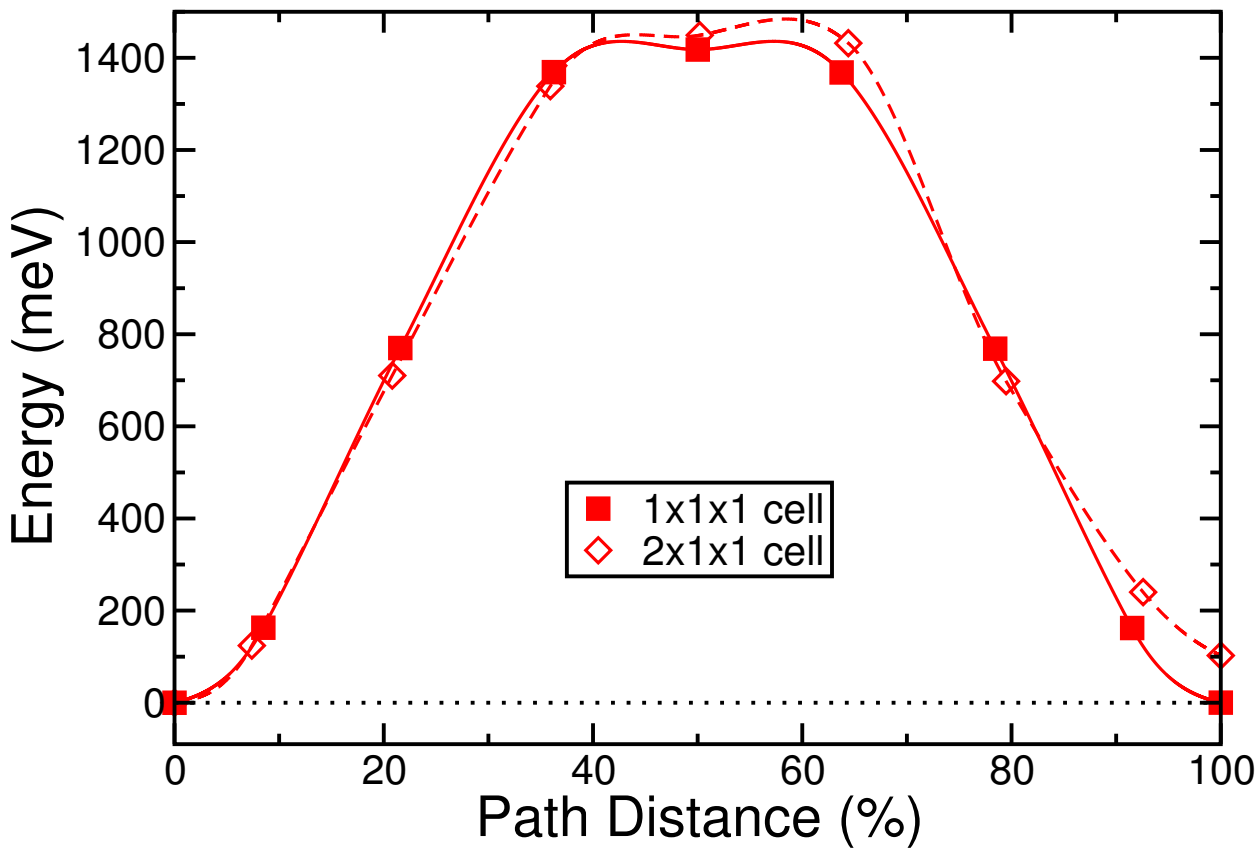

Figure S2: Variation of Mg activation barriers with cell size used in the Nudged Elastic Band calculations

the barrier. The energy difference between the initial and final states in the 2×1×1 cell ($\sim$ 100 meV) is due to the asymmetry of the cation occupancy in the 16d sites between the end points, while the 1×1×1 cell does not display any such asymmetry.

3 Nudged Elastic Band data for $MgMn_2O_4$

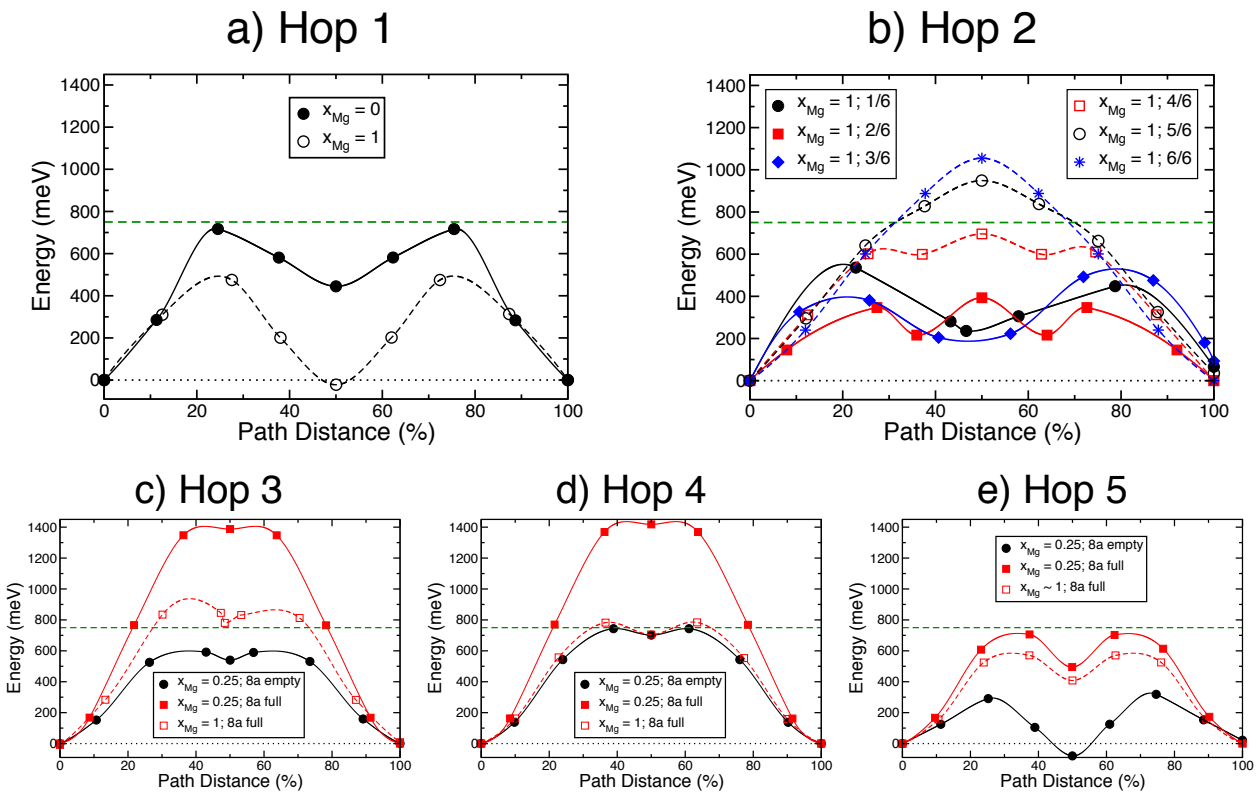

Figure S3: Activation barriers for Mg^{2+} diffusion in normal and inverted spinel-Mn_2O_4 under different local environments. The dashed green lines in all panels represent the upper-bound of the migration barrier for a $\sim$ 100 nm ($\sim$ 750 meV) cathode particle being (dis)charged at a C/3 rate. The dotted black lines indicate zero, where zero is referenced to the lowest energy among the initial and final end points. The fractions in panel (b) indicate Mg occupancy of the 16d "ring" sites (refer Section 2.1 in the main text). The legends "8a full" and "8a empty" in panels (c), (d), and (e) indicate that the 8a sites that corner-share with the intermediate 48f are cation-occupied and vacant, respectively. x_{Mg} in all panels refers to the Mg concentration at which the corresponding barrier has been calculated. For the specific case of 1/6 Mg ring site occupancy in Hop 2 (solid black line in panel b), we used 5 images between the end points due to convergence issues while using 7 images.

4 Nudged Elastic Band data for $MgIn_2S_4$

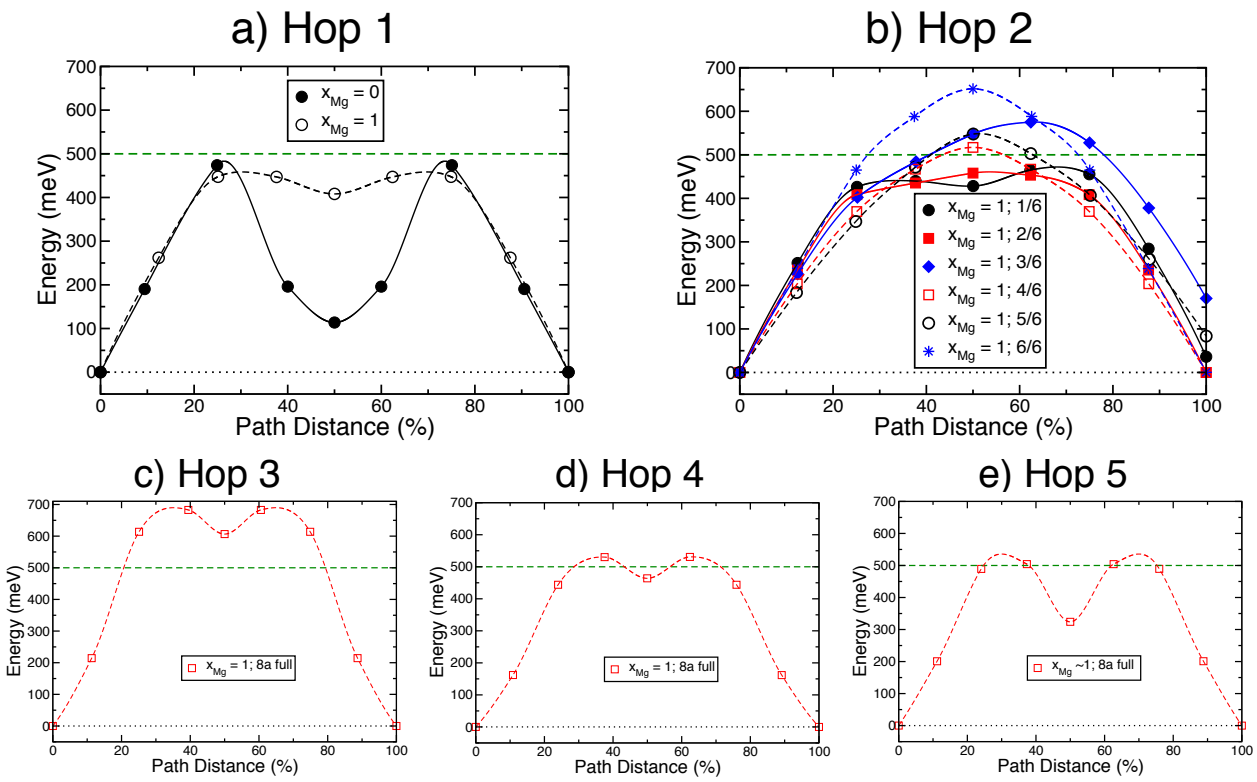

Figure S4: Activation barriers for Mg^{2+} diffusion in normal and inverted spinel-In_2S_4 under different local environments. The dashed green lines in all panels represent the upper-bound of the migration barrier for a reasonable solid electrolyte ($\sim$ 500 meV), while the dotted black lines indicate zero. The zero energy in each panel is referenced to the lowest energy among the initial and final end points, which should be ideally identical. However, similar to Figure S3, there are scenarios with a non-negligible difference between the end point energies, which is due to the symmetry of the cation arrangement being broken differently between the end points. The fractions in panel (b) indicate Mg occupancy of the 16d "ring" sites. The legends "8a full" in panels (c), (d), (e) indicates that the 8a sites that corner-share with the intermediate 48f are cation-occupied. x_{Mg} in all panels refers to the Mg concentration at which the corresponding barrier has been calculated.

5 Activation barrier along Hop 4 in Mn-spinel

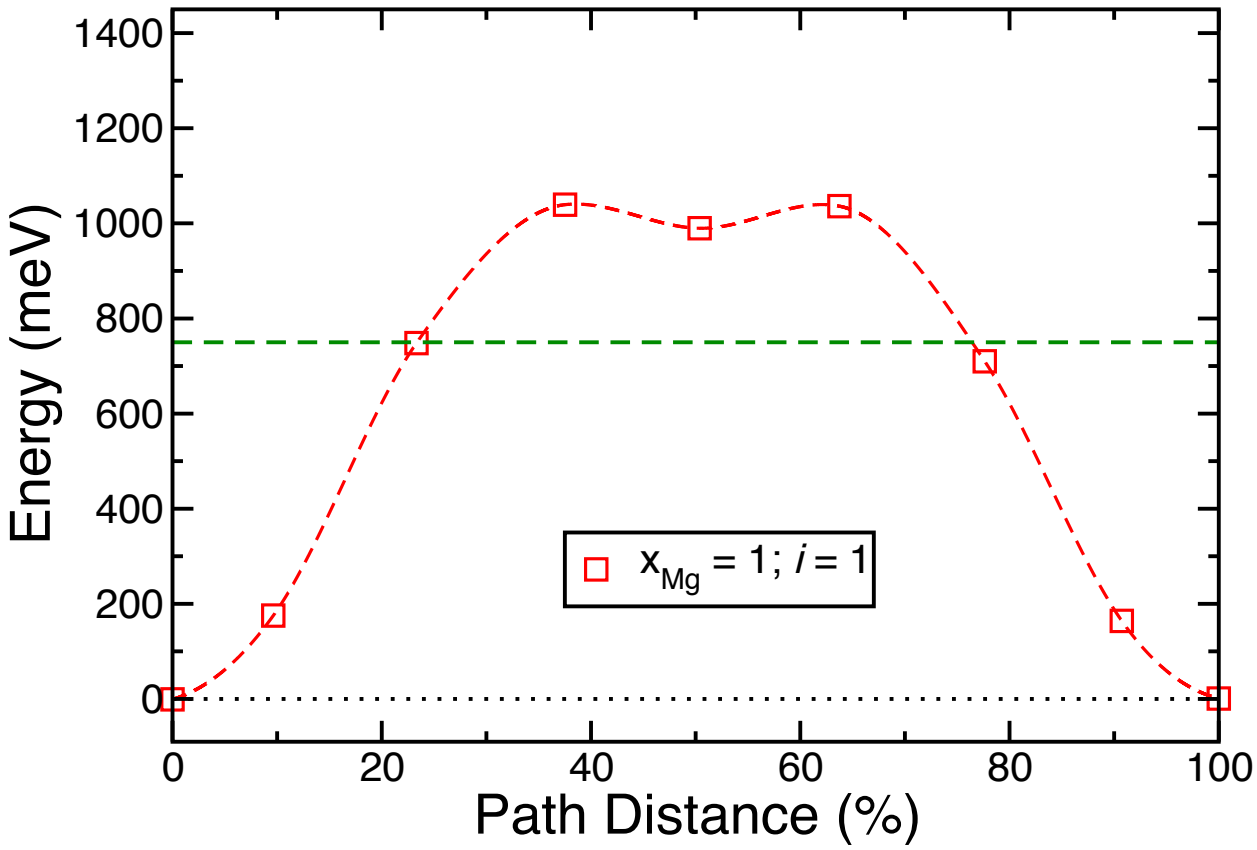

Figure S5: Activation barrier for Mg^{2+} diffusion along the Hop 4 trajectory ($16d-48f-16d$ with Mn in edge-$8a$, Figure 2d in the main text) at $x_{Mg} = 1$ and $i \sim 1$ in the $MgMn_2O_4$ spinel structure. The dashed green line (750 meV) indicates the barrier thresholds used in percolation simulations (see Section 4, main text).

6 Convergence of Monte-Carlo percolation simulations

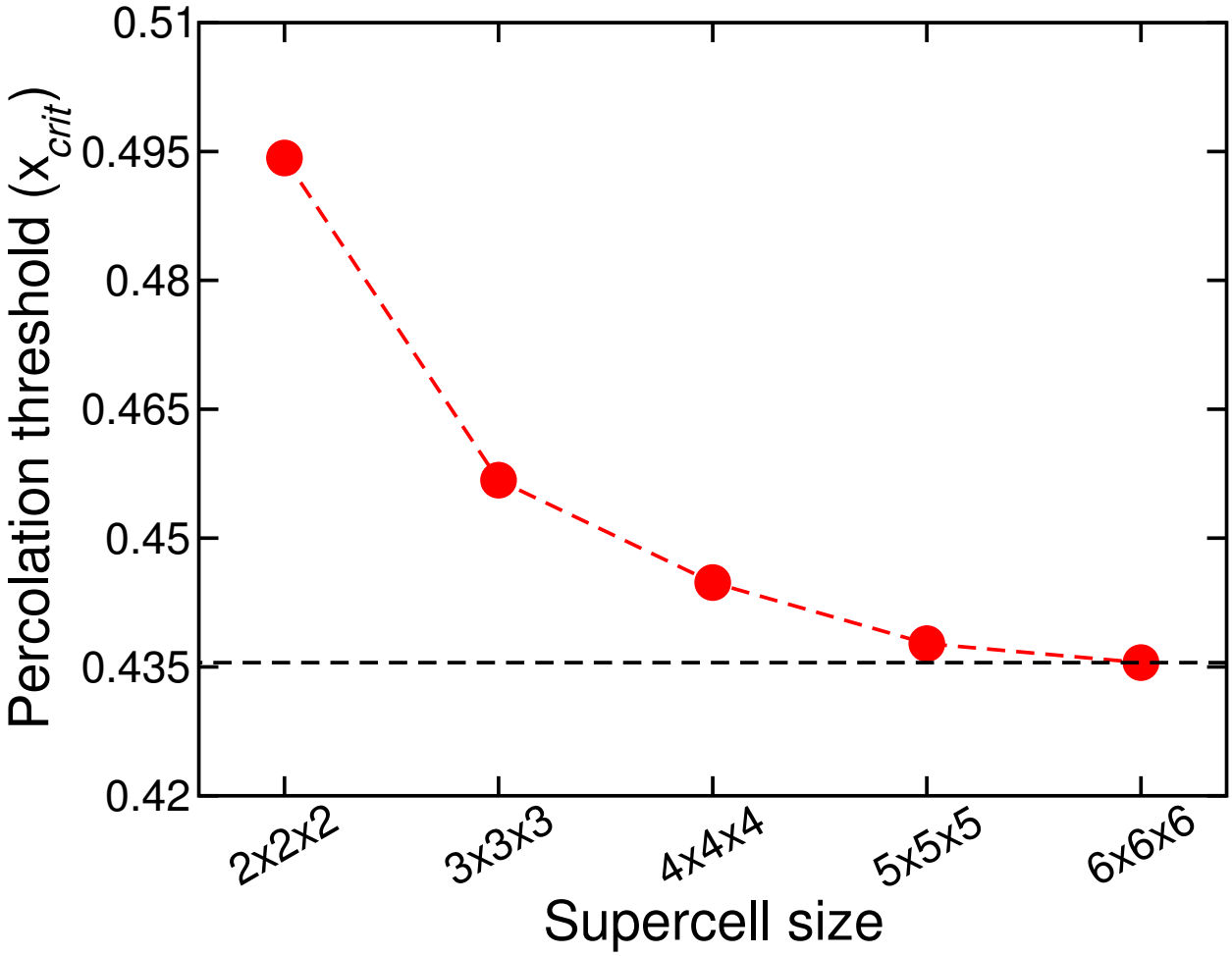

Figure S6: The convergence of percolation thresholds (x_{crit}, Section 2.2 in the main text), with supercell size during Monte-Carlo simulations. The cells are initialized with a M_3X_4 stoichiometry (i.e., no vacancies) and scanned for percolating Mg networks (as detailed in Section 2.2). The supercell size indicated is with respect to the primitive spinel cell, which is equivalent to 8 anion atoms. A 6×6×6 supercell (1728 anions) is used in further x_{crit} estimations, since the difference in thresholds between a 5×5×5 and a 6×6×6 supercell is $< 1\%$.

7 Varying vacancy concentration in percolation simulations

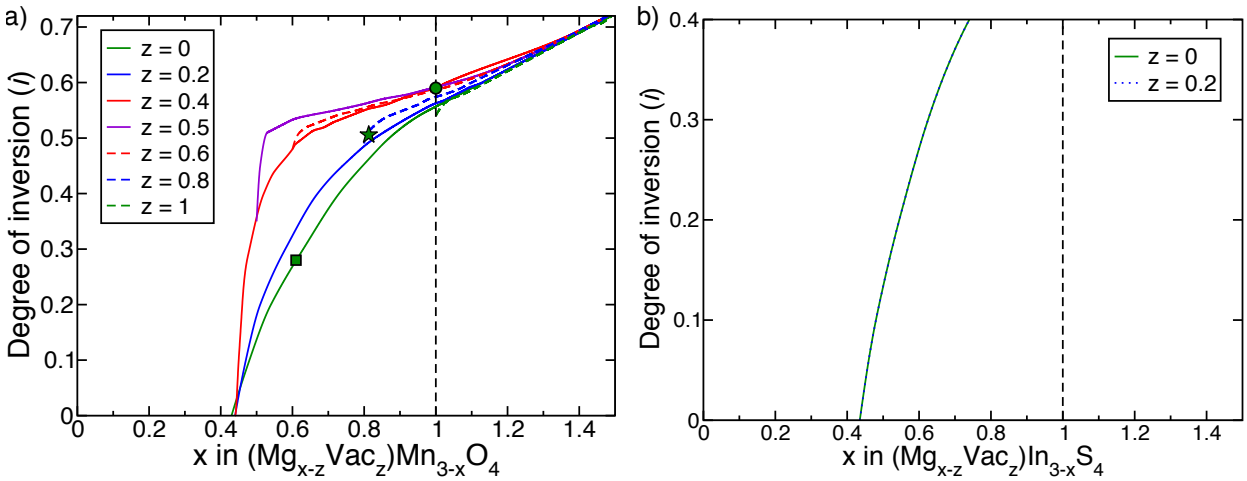

Figure S7: Percolation thresholds calculated with different initial vacancy concentrations are plotted for $(Mg_{x-z}Vac_z)Mn_{3-x}O_4$ (a) and $(Mg_{x-z}Vac_z)In_{3-x}S_4$ (b). The x-axis corresponds to the total deficiency of M (M = Mn/In). During Monte-Carlo simulations, structures are initialized with different concentrations of vacancies (legends "z") in the Mg sub-lattice, leading to initial stoichiometries of $Vac_zMn_{3-z}O_4$, followed by flipping the Mn sites to Mg until the formation of a percolating network (see Section 2.2 and Section 4.3 in the main text). Thus, for a given value of z, the total M deficiency is at least equal to the vacancy content, i.e., $x \geq z$. Therefore, at a given i and z, the x_{crit} is plotted only if $x_{crit} > z$. The dashed black lines in both panels indicates the stoichiometric spinel. The z = 0 (solid green) and z = 0.2 (dotted blue) lines in panel b display the same numerical trends. The green circle, square and star symbols in panel a correspond to the sample scenarios discussed in Section 4.3 of the main text.

8 $16d - 8a$ hops in $MgMn_2O_4$ and $MgIn_2S_4$

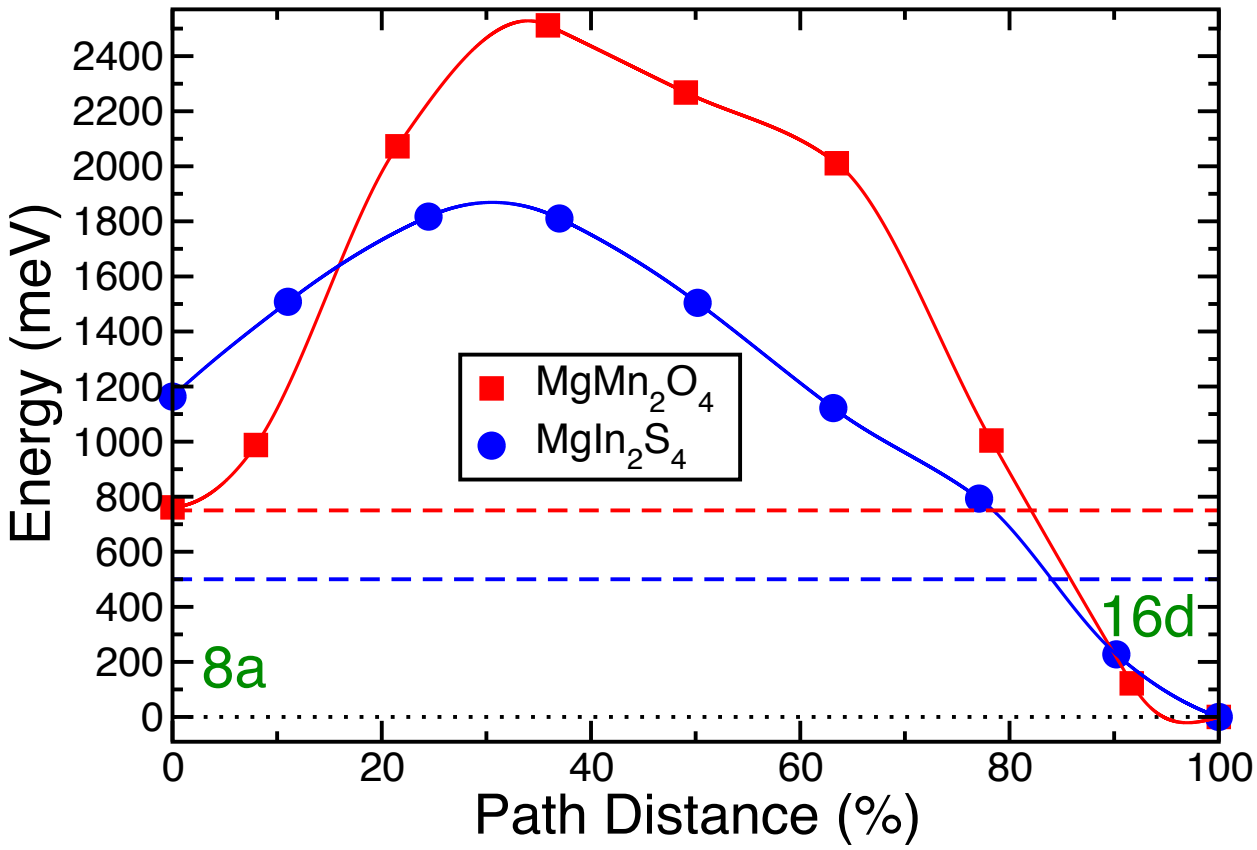

Figure S8: Mg^{2+} activation barrier for diffusion from a $8a$ *tet* (0% on the x-axis) to a $16d$ *oct* (100%) site for $Mg_xMn_2O_4$ (at $x_{Mg} \sim 0$, red) and the $MgIn_2S_4$ (at $x_{Mg} \sim 1$, blue) spinel structures. The dashed red (750 meV) and blue (500 meV) indicate the barrier thresholds used in percolation simulations for cathode-$Mg_xMn_2O_4$ and ionic conductor-$MgIn_2S_4$, respectively, indicating that the $8a - 16d$ hops will not participate in any percolating Mg^{2+} network in both the oxide and the sulfide spinel. Interestingly, the $8a$ site becomes highly unstable in the presence of a vacant corner-sharing $16d$ site, as demonstrated by the higher energy of the $8a$ compared to $16d$ in both the Mn- and In-spinel. Additionally, the $8a - 16d$ barriers indicate that a given percolating network in the oxide or sulfide spinel will be composed exclusively of either $8a - 8a$ or $16d - 16d$ diffusion channels, and not a mix of both.

9 Mobility of Mn^{2+} in Mn_2O_4

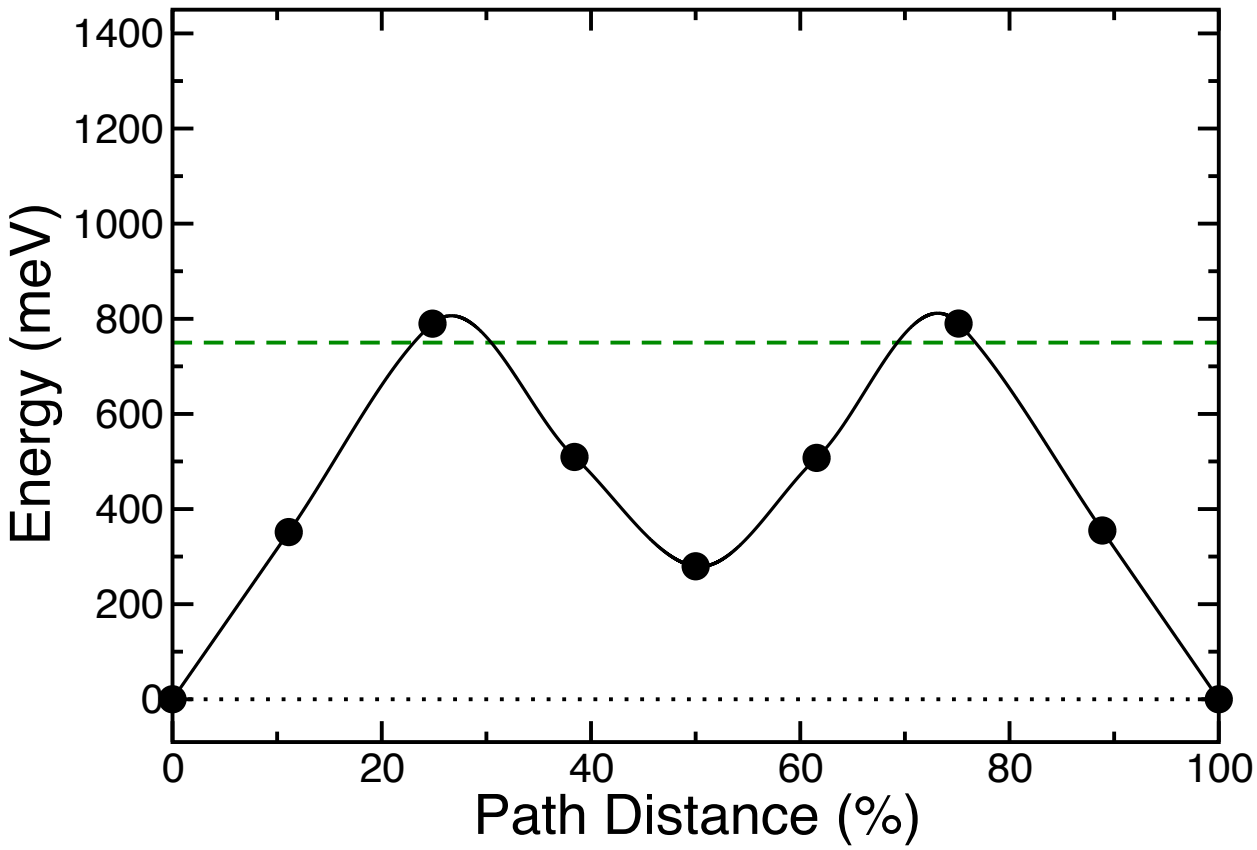

Figure S9: Mn^{2+} diffusion barrier along a "Hop 1" pathway ($8a - 16d - 8a$, Figure 2a in the manuscript), with the stoichiometry of the spinel corresponding to $Mn_{\sim 0}Mn_2O_4$. The dashed green line (750 meV) indicates the barrier thresholds used in percolation simulations, suggesting that Mn^{2+} migration along the Hop 1 trajectory might be comparable to Mg^{2+} diffusion along the same pathway ($\sim$ 716 meV barrier for Mg^{2+} along Hop 1 in the dilute Mg limit, Figure 3a of main text). Mobile Mn^{2+} ions, generated by the disproportionation Mn^{3+}, can cause a change in the degree of inversion during electrochemical cycling of Mg.

10 Ground state hull: $Mg_xMn_2O_4$

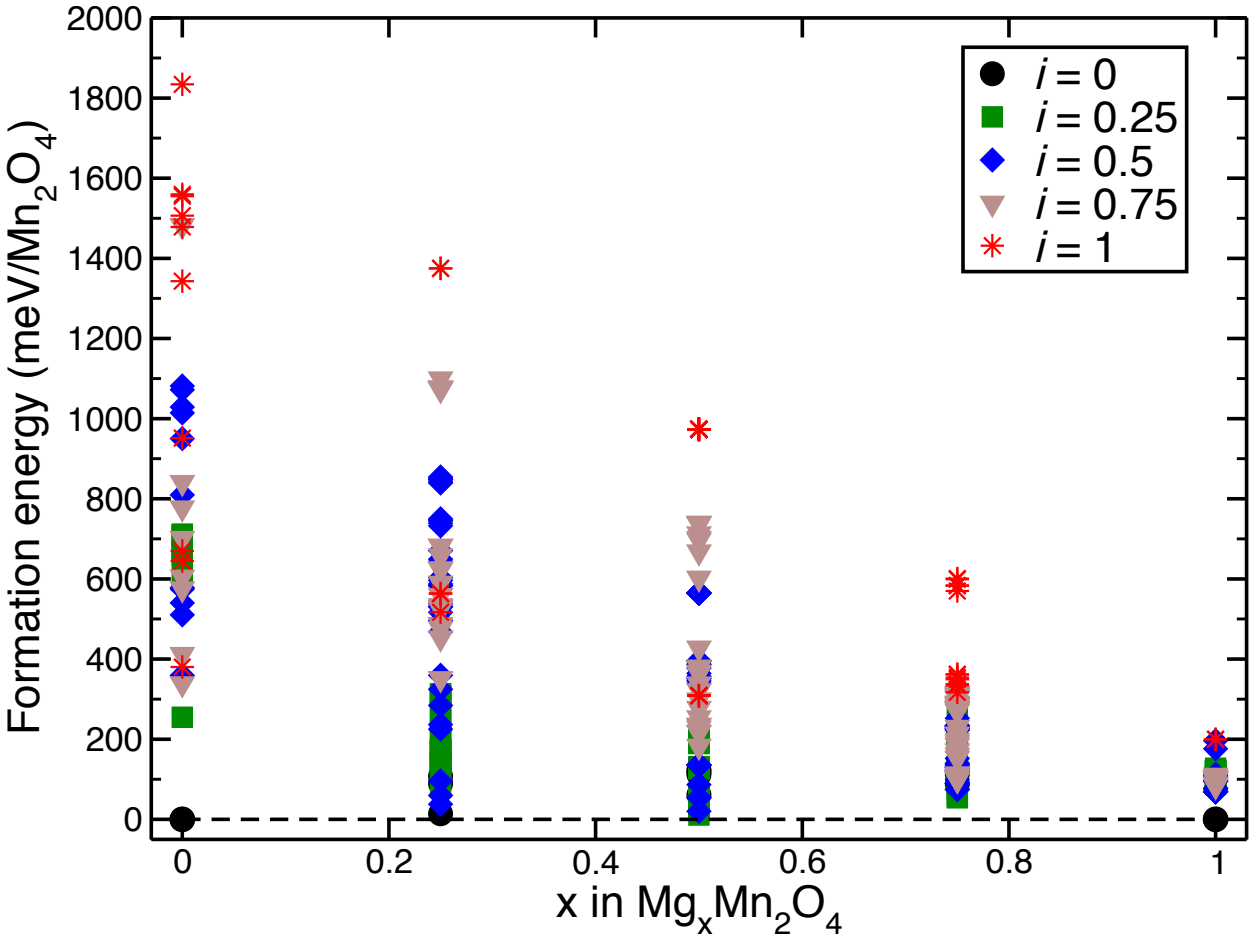

Figure S10: Ground state hull, or the 0 K phase diagram of the $Mg_xMn_2O_4$ system, with calculations done at different Mg concentrations (x) and degrees of inversion (i). The zero of the formation energy scale is referenced to the $i = 0$, fully magnesiated ($MgMn_2O_4$) and empty (Mn_2O_4) spinel configurations. The DFT energies of $\sim$ 400 Mg-vacancy orderings within the conventional spinel cell (32 oxygen atoms) are used to construct the hull. The structure-enumeration algorithms,[1–3] as implemented in the pymatgen library,[4] are used to generate the various Mg-vacancy orderings.

11 Inversion energetics in $MgIn_2S_4$

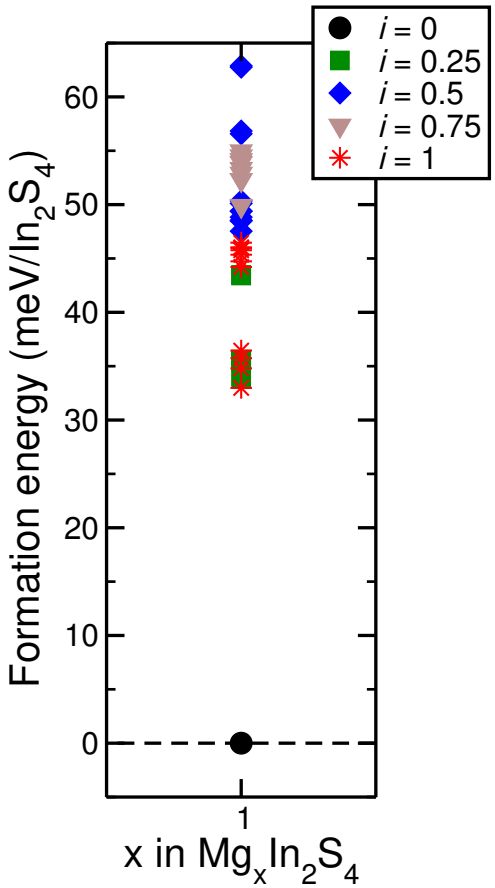

Figure S11: The formation energy at 0 K of inverted spinel-$MgIn_2S_4$, with configurations considered at different degrees of inversion (i). Since $MgIn_2S_4$ is an ionic conductor, we consider the energy to invert the spinel only at $x_{Mg} = 1$ (i.e., at the stoichiometry of $MgIn_2S_4$). The zero of the formation energy scale is referenced to the non-inverted spinel configuration. The DFT energies of $\sim$ 40 Mg-In inversion orderings within the conventional spinel cell (32 sulfur atoms) were generated via structure-enumeration algorithms[1–4] and were calculated as detailed in Section 3 of the main text. Comparing the formation energies of inverted structures of $MgMn_2O_4$ (x = 1 in Figure S10 and Figure 6a in the main text) and $MgIn_2S_4$, we note that inversion should be easier to introduce in spinel-$MgIn_2S_4$ than the oxide spinel, due to the presence of lower formation energy inverted structures ($\sim$ 35 meV/f.u. in the In-spinel compared to $\sim$ 70 meV/f.u. in the Mn-spinel).

12 Structural distortion in spinel-$Mg_xMn_2O_4$

Table S4: Lattice parameters (in Å) and the c/a ratio, obtained through DFT calculations (methods outlined in Section 3 of the main text) and experiments, for tetragonal-$MgMn_2O_4$ and cubic-Mn_2O_4. For the sake of comparison, the tetragonal (space group: $I4_1/amd$) and the cubic ($Fd\bar{3}m$) structures, the lattice parameters of the tetragonal spinel are changed to represent a bigger supercell, i.e., $a'_{tetragonal} = a_{tetrgonal} \times \sqrt{2}$.

Composition	c	a'	c/a'	Source
$MgMn_2O_4$	9.267	8.148	1.147	Theory (this work)
	9.284	8.099	1.146	Experiment[5,6]
Mn_2O_4		8.128	1.0	Theory (this work)
		8.081	1.0	Experiment (for $Li_{0.2}Mn_2O_4$)[7]

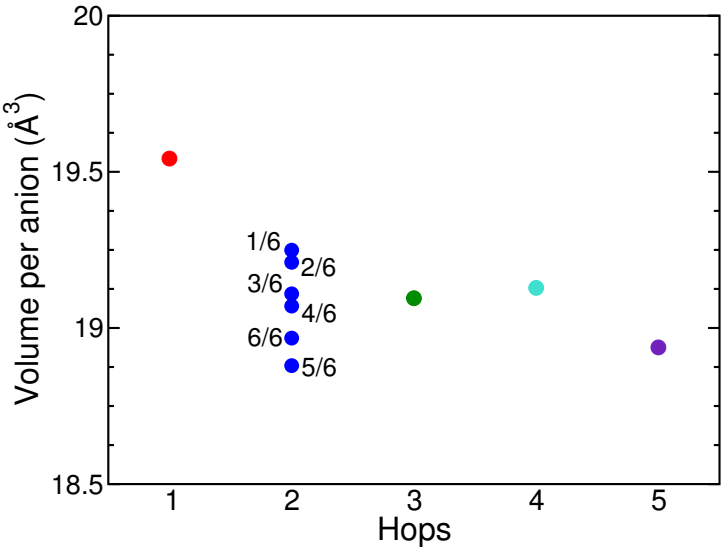

Figure S12: The volume per anion (in Å^3) for structures used to model the various Mg-hops in spinel-$Mg_xMn_2O_4$ are plotted. All volumes are taken at the dilute vacancy ($x_{Mg} \sim 1$) limit. The fractions along Hop 2 indicate the fraction of ring sites occupied by Mg (similar to the notation used in Figure 3 of the main text). It has been shown experimentally that the tetragonal-$MgMn_2O_4$ spinel becomes cubic at high degrees of inversion.[6] Consequently, the volume along Hop 2 decreases monotonically with increasing degree of inversion, resulting from an increasing Mg occupancy of the ring sites (see Section 3 of the main text).

13 Configurations considered for Hop 2 in $MgMn_2O_4$ and $MgIn_2S_4$

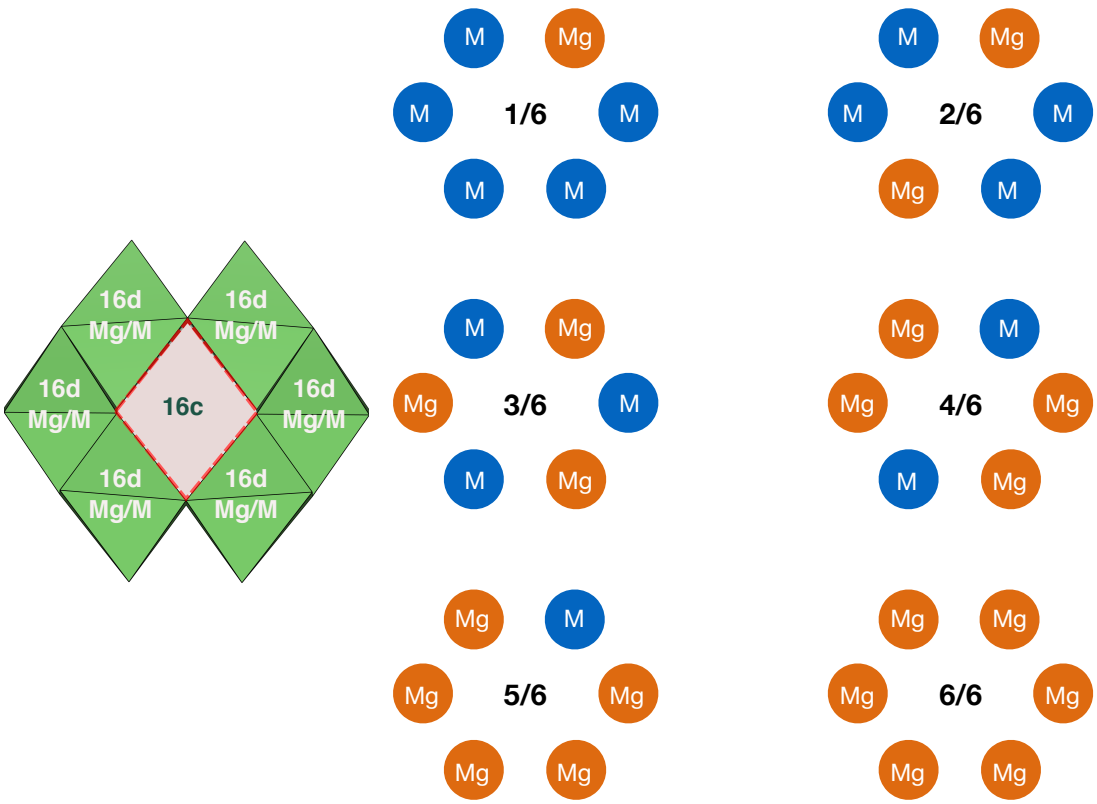

Figure S13: The cation arrangements used to evaluate Mg migration barriers along Hop 2 (Figure 2b in main text) in $MgMn_2O_4$ and $MgIn_2S_4$. The orange and blue circles indicate Mg and M (M = Mn/In) atoms occupying a 16d ring site. The fraction indicated within each configuration corresponds to the fraction of the ring sites that are occupied by Mg. Each configuration displayed here exhibits the lowest electrostatic energy (i.e., lowest electrostatic repulsions) for the corresponding Mg ring-site occupancy.

14 Vacancies in 16d ring sites along Hop 2 in $Mg_xMn_2O_4$

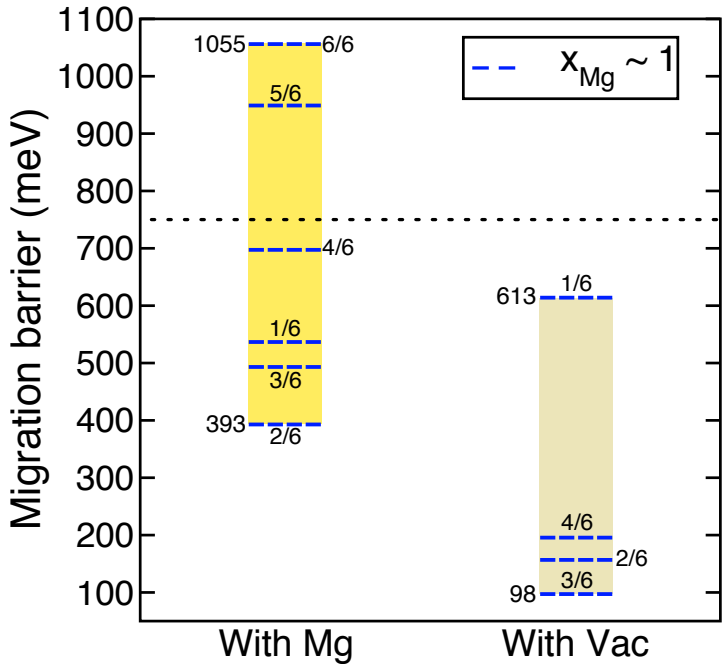

Figure S14: Ranges of Mg^{2+} migration barriers along Hop 2 (Figure 2b in main text) in spinel-$Mg_xMn_2O_4$. The dotted black line indicates the upper-limit of migration barriers ($\sim$ 750 meV) used to distinguish open and closed migration channels in percolation simulations. Dashed blue lines correspond to dilute vacancy ($x_{Mg} \sim 1$) limit. Fractions on the plot indicate the occupancy of Mg^{2+} or Vacancy (Vac) in the 16d ring sites. Along Hop 2, i varies with Mg/Vac occupancy of the ring sites, ranging from $i \sim 0.125$ at 1/6 Mg (or Vac) to $i \sim 0.75$ at 6/6 Mg (Vac). The same cation arrangements displayed in Figure S13 are used for calculations involving vacant ring sites, with the Mg atoms (orange circles in Figure S13) being replaced by Vac. Notably, Hop 2 remains active until 4/6 occupation of ring site by both Mg and Vac. Due to convergence issues in our calculations, we are unable to estimate the migration barriers at 5/6 and 6/6 Vac. However, high vacancy concentrations on the ring sites, such as 5/6 and 6/6 Vac, are unlikely due to the high formation energies (>200 meV/f.u.) of highly inverted configurations ($i > 0.5$) at low Mg concentrations ($x_{Mg} < 0.5$) in Figure 6a and Figure S10. Thus, both Mg and Vac are expected to display identical behavior in determining open and closed channels, when occupying the ring sites along Hop 2.

References

(1) Hart, G.; Forcade, R. Algorithm for generating derivative structures. *Phys. Rev. B* **2008**, *77*, 224115.

(2) Hart, G.; Forcade, R. Generating derivative structures from multilattices: Algorithm and application to hcp alloys. *Phys. Rev. B* **2009**, *80*, 014120.

(3) Hart, G. L.; Nelson, L. J.; Forcade, R. W. Generating derivative structures at a fixed concentration. *Comput. Mater. Sci.* **2012**, *59*, 101–107.

(4) Ong, S. P.; Richards, W. D.; Jain, A.; Hautier, G.; Kocher, M.; Cholia, S.; Gunter, D.; Chevrier, V. L.; Persson, K. A.; Ceder, G. Python Materials Genomics (pymatgen): A robust, open-source python library for materials analysis. *Comput. Mater. Sci.* **2013**, *68*, 314–319.

(5) Sanjana, N.; Biswas, A.; Sinha, A. Crystal Structure of Magnesium Manganate, $MgMn_2O_4$. *J. Sci. Ind. Res. B* **1960**, *19*, 415–9.

(6) Irani, K.; Sinha, A.; Biswas, A. Effect of temperature on the structure of manganites. *J. Phys. Chem. Solids* **1962**, *23*, 711–727.

(7) Kim, C.; Phillips, P. J.; Key, B.; Yi, T.; Nordlund, D.; Yu, Y.-S.; Bayliss, R. D.; Han, S.-D.; He, M.; Zhang, Z. et al. Direct Observation of Reversible Magnesium Ion Intercalation into a Spinel Oxide Host. *Adv. Mater.* **2015**, *27*, 3377–3384.